Physics-informed neural networks for predicting deformation and stress fields in asymmetric composite adhesive joints

Zewen Gu[a, *], Yalong Liu[a], Xiaoxuan Ding[a, *], Jianwei Zhao[b], Jianlin Liu[a], Jianqiao Ye[c], Xiaonan Hou[c]

[a] *Department of Engineering Mechanics, College of Pipeline and Civil Engineering, China University of Petroleum, Qingdao, 266580, Shandong, China*

[b] *School of Mechanical Engineering, University of Science and Technology Beijing, 100083, Beijing, China*

[c] *School of Engineering, Engineering Building, Lancaster University, Lancaster, LA1 4YW, United Kingdom*

Abstract

The widespread use of composite adhesive joints in aerospace, automotive, and advanced technological applications is attributed to their lightweight nature and specific strength relative to metals and mechanical fasteners. However, the nonlinear loading conditions within the adhesive layer pose significant challenges for accurately predicting joint strength and stress distribution. This study integrates experiments, finite element analysis (FEA), theoretical modeling, and physics-informed neural networks (PINNs) to predict deformation and stress fields in bonded joints under tensile loading. Tests and simulations on CFRP–CFRP and Al–CFRP joints were conducted to validate the FEA model. Based on these results, PINNs using Timoshenko beam theory and two-dimensional elasticity were developed to predict deformation and stress fields, respectively. Both frameworks demonstrated high accuracy, particularly in asymmetric and mixed-material joints where nonlinearities dominate. R^2 remained above 0.85, with displacement errors below 0.1 mm and stress field errors under 5%. The proposed method offers a fast, reliable approach for predicting joint strength by overcoming the difficulty of solving partial differential equations under complex nonlinear loads. This work advances the understanding of adhesive joint mechanics and highlights the potential of PINNs for solving complex governing equations, providing a powerful framework for future research on intricate joint structures.

Keywords:

Composites adhesive joints; physical-information neural networks; Partial differential equations; Theoretical model; Finite element analysis

1.Introduction

Bonded joints, particularly those involving composite materials, are fundamental joining solutions in modern engineering, with extensive applications spanning aerospace [1, 2], automotive [3], and advanced technologies such as superconducting tapes and thin films [4, 5]. In contrast to mechanical fastening, adhesive bonded joints preserve the structural integrity of the adherends and contribute substantially to overall weight reduction [6]. The relatively low elastic modulus and inherent viscoelastic of the adhesive layer further provide excellent vibration damping and impact resistance [7]. Additionally, the sealed interface formed during adhesive curing enhances corrosion protection [8, 9]. Given that the joint is often the most failure-prone component in such structures, accurate prediction of its strength remains a critical priority in engineering design and assessment.

Analytical models provide a streamlined and practical means of predicting joint strength. Their development traces back to foundational theories that introduced key concepts such as peel stress and bonding corner angles [10]. Despite their innovation, early models relied on simplified assumptions, such as neglecting adhesive layer thickness and shear strain. In response to the limitations of early models, subsequent research was conducted for analyzing the joint as three discrete components rather than as a whole [11], developing specialized models for long joints [12], and formulating models based on a linear through-thickness shear stress distribution [13, 14]. Driven by specific application needs, further models have been developed for different types of adherends, including composites [15] and gradient materials [16, 17]. While these models primarily focus on stress distribution within the adhesive layer, it remains a lack of efficient analytical models capable of predicting full-field stress-strain distribution across the entire joint.

In this context, the stress-strain field of entire joints region can be derived from established beam theories by idealizing the joint as two coupled beams [18]. Exact analytical solutions for such beams are usually available under uniformly [19], quadratic [20, 21] and sinusoidal [22] distributed loads. It should be noted that the loads (or adhesive stress in joints) in these models are simplified to linear or trigonometric functions, which cannot represent the far more complex loading conditions in adhesive bonded joints. In practice, however, the load distributed on the adherends originates from the adhesive layer's stress field, which is typically highly nonlinear [23, 24]. The core challenge is that extending beam models to a two-dimensional configuration introduces a significant additional solving difficulties, as it requires deriving an accurate Airy stress function that fully captures the behavior of joints [25].

In recent years, data-driven approaches powered by machine learning offer a promising alternative to solve such complicated problems. Its applications extend across multiple fields, including predicting composite material properties [26, 27], optimizing manufacturing processes [28, 29], and supporting failure analysis [30-32]. However, purely data-driven models often face limitations of data dependency and lack of physical interpretability. The physics-informed neural networks (PINNs) framework effectively avoids this problem. PINNs was originally introduced as a novel methodology for solving forward and inverse problems governed by partial differential equations [33], and has since been applied to areas such as high-dimensional problems and nonlinear dynamics [34-38]. As the application scope continues to expand, PINNs has also played a significant role in the field of solid mechanics [39, 40]. Recent works successfully applied it to both forward and inverse problems in solid mechanics [41], with subsequent efforts employing hierarchically normalized PINNs to resolve training instability [42]. Simultaneously, the model has been optimized through different techniques to ensure robust performance under a wider range of complex conditions. [43, 44]. In the field of composite materials, one study combined PINNs with self-consistent cluster analysis to efficiently predict the nonlinear mechanical response of unidirectional CFRP RVEs, achieving high accuracy while cutting computational costs several-fold compared with conventional methods [45]. A separate study integrated first-order shear deformation theory and transfer learning into a PINN framework to enable high-precision identification of composite laminate material parameters [46]. Collectively, these advancements have promoted physics-informed neural networks into a powerful computational tool capable of integrating physical laws with sparse data, thereby making it well-suited for complex engineering scenarios [47]. As outlined above, the powerful PINNs framework holds considerable promise as a robust approach to joint problems, while dedicated studies in this area are currently lacking.

This study focuses on the difficulty of solving the governing equations for adhesive joint strength prediction under nonlinear loads applied to the bonded region. The mechanical properties and ply orientation of the carbon fiber reinforced polymer (CFRP) were first characterized experimentally. Two types of adhesive-bonded joints were then fabricated and tested under uniaxial tension. A finite element model was subsequently developed and validated against the experimental results. Based on different theoretical assumptions, the governing equations for the adherends in the bonded joints were analytically derived. To overcome the difficulty of solving these equations directly, one-dimensional and two-dimensional PINNs frameworks were established in accordance with the aforementioned theories. The validated finite element model was employed to generate training data for the PINNs frameworks, which were then used to predict the

mechanical responses for new geometric parameters. Finally, the PINNs predictions were compared with the corresponding finite element results to assess their accuracy and reliability.

2. Experiments and Numerical Model

2.1 Material property testing and tensile testing

The bonded components in this study consisted of an aluminum alloy (supplied by Kunshan Chenyituo Aluminum Co., Ltd., Kunshan, China) and a T300 carbon fiber reinforced polymer (CFRP) (using carbon fiber tows from Toray Industries, Inc., Japan). The adhesive used was Araldite® 2015. The CFRP laminates were manufactured via autoclave curing, and scanning electron microscope (SEM) analysis confirmed a 0°/90° cross-ply fiber arrangement. Standard specimens were prepared to evaluate the mechanical properties of the cured material, and the adhesive parameters were taken from the technical data sheet for Araldite 2015 issued by Huntsman (USA), with the corresponding results summarized in Table 1. Each adherend measured 150 mm × 25 mm × 5 mm, and the adhesive layer thickness was controlled at 0.5 mm over a bonding length of 50 mm. Tests were conducted on two adherend configurations: CFRP-CFRP and Al-CFRP. Five replicate tests were performed for each configuration to ensure result consistency.

Table 1. Detailed material parameters of adhesives and adhesives.

	Aluminum alloy	CFRP	Araldite 2015
Young modulus (MPa)	71,000	69,000	1,600
Shear modulus (MPa)	26,692	28,750	620
Poisson's ratio	0.33	0.2	0.29

To ensure optimal bonding quality, the adherend surfaces were treated by sandblasting to increase roughness (abrasive particle size: 150-250 μm) and subsequently the surface stains were removed by washing with acetone. The adhesive layer thickness was controlled to 0.5 mm using copper wires of the same diameter. Balance blocks measuring 25 mm × 25 mm × 5 mm were attached at both ends of the joint to facilitate tensile testing. The assembly was then clamped and allowed to cure for 48 hours at 26 °C and 100.9 kPa to ensure complete adhesive curing.

The strength of adhesive-bonded joints was primarily evaluated by uniaxial tensile testing, as illustrated in Figure 1(b). In this configuration, the load was applied perpendicular to the adhesive plane and passed through the center of the bonded area. All tests were conducted using an LE5105-H800 universal testing machine under quasi-

static conditions, with a constant crosshead speed of 1.2 mm/min. A speckle pattern was applied on one side of the specimen for digital image correlation (DIC) analysis using an RTTS-100D system, at a temperature of 24°C and a pressure of 101kPa. The resulting force-displacement curves and displacement nephogram were used to validate the accuracy of subsequent numerical models and PINNs models.

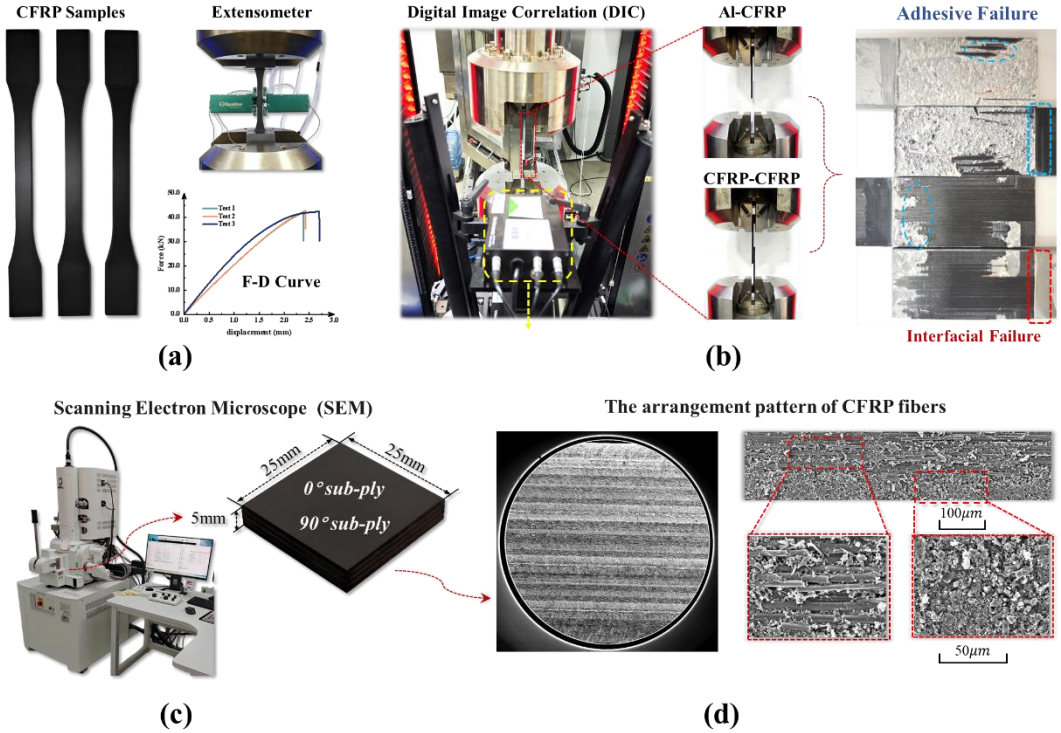

Figure 1. Experimental content schematic diagram.

2.2 Development of the finite element model

To supplement the experimental data for subsequent machine learning models, a finite element model under plane strain conditions was established using ANSYS Workbench. Based on the plane strain simplification, justified by the fact that the adhesive layer width significantly exceeds its thickness and the surrounding adhesive strongly constrains out-of-plane deformation, the out-of-plane strain is effectively forced to zero. Furthermore, this assumption is grounded in the Engineering Sciences Data Unit (ESDU) and SAE International ARP 4977, which likewise recommend the use of a plane-strain framework for modeling. Specifically, the energy-based debonding CZM uses a bilinear traction–separation law. The initial linear elastic branch is governed by the contact stiffness, followed by a linear softening branch controlled by the mixed-mode fracture energy. This behavior is characterized by four key parameters: the maximum normal contact stress, the maximum equivalent tangential contact stress, the critical fracture energy for normal separation (G_IC), and the critical fracture energy for tangential slip ($G_{II}C$). Their specific values are provided in Table 2 [48].

Table 2. Finite element model CZM parameter settings.

Property	Araldite 2015
Tensile failure strength (MPa)	21.63 ± 1.61
Shear failure strength (MPa)	17.9 ± 1.8
Tensile yield strength (MPa)	12.63 ± 0.61
Shear yield strength (MPa)	14.6 ± 1.3
G_IC (N/mm)	0.43 ± 0.02
$G_{II}C$ (N/mm)	4.7 ± 0.34

The finite element mesh, depicted in Figure 2, consisted predominantly of second-order, eight-node quadrilateral elements with a displacement-based formulation. Local refinement was implemented in the adhesive layer and along the bonded edges to accurately capture the stress distribution. Due to the parametric nature of the model, the number of elements varies with the structural dimensions; for the symmetric lap joint configuration, for instance, the total number of elements was 22,668. In the analysis, geometric nonlinearity is enabled to account for large deformations, thereby improving the physical realism of the simulation. The boundary conditions replicate those used in the experiment: one end of the specimen is fully clamped, while the other end is constrained against displacement in the y-direction and rotation about the z-axis, allowing displacement only in the x-direction. The output of the numerical model was twofold. The first part was the force-displacement curve at the fixed end, which served to validate the accuracy of the finite element model by comparing it with the experimental data. The second part was dedicated to generating training data for the PINNs. Specifically, the adherends were divided into multiple layers, and a set number of data points were extracted from each layer as outputs, ultimately forming an n × m output matrix.

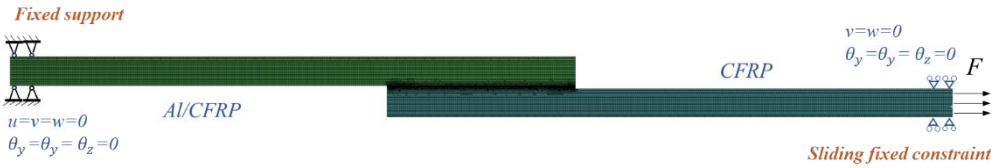

Figure 2. Schematic diagram of the finite element model.

3. Theoretical models

During tension of adhesive joints, rotation occurs in the bonded region because of the

eccentric effect arising from the non-collinear load path. This, as explained previously, greatly increases the complexity of analyzing the adherends. A viable strategy to overcome this difficulty is to separate the bonded joint into individual components. By exposing stress distribution within the adhesive layer and applying it as an external load on the adherends. As a result, the bonded joint can be simplified as a cantilever beam model subjected to distributed loading. A schematic of this configuration is shown in Figure 3. Where h_a, h_b, and h_0 are the thicknesses of the upper adherend, lower adherend, and adhesive layer; E_a, E_b, and E_0 are the corresponding elastic moduli; and v_a, v_b, and v_0 are the Poisson's ratios. L is the adherend length, and l is the adherend length.

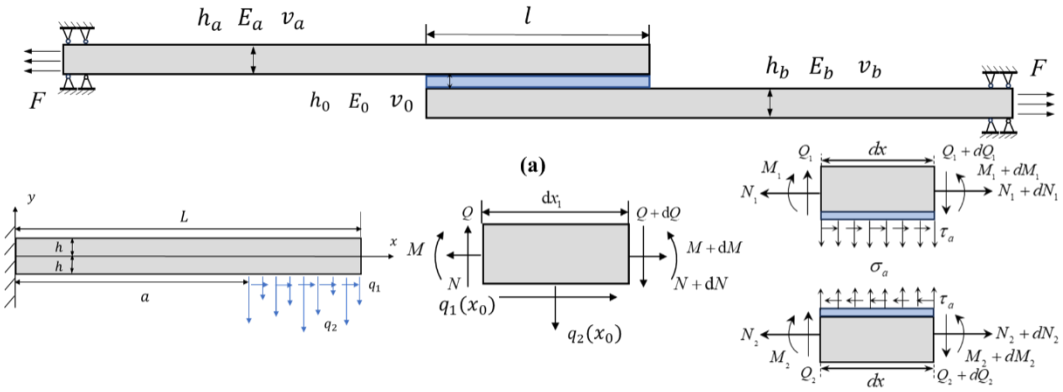

Figure 3. Structure of the adhesive joint and simplified schematic diagram.

3.1 Deflection curve model for adhesive joints based on Timoshenko beam theory

In the Timoshenko beam model, shear deformation is assumed to be linearly distributed. This stems from the hypothesis that cross-sections remain planar during deformation, in that they do not stay normal to the deformed centroidal axis but rather experience a distinct rotation. Its displacement equation is:

$$u_i = \begin{cases} u_1(x_1, x_2) = u_0(x_1) + x_2\theta(x_1) \\ u_2(x_1, x_2) = w_0(x_1) \end{cases} \tag{1}$$

The expression of the strain tensor and its various components is:

$$\varepsilon_{ij} = \frac{1}{2}\left(\frac{\partial u_i}{\partial x_j} + \frac{\partial u_j}{\partial x_i}\right) \tag{2}$$

The result obtained by substituting the above displacement equation is:

$$\varepsilon_{11}=\frac{\partial u_1}{\partial x_1}=\frac{\mathrm{d}u_0}{\mathrm{d}x_1}+x_2\frac{\mathrm{d}\theta}{\mathrm{d}x_1}$$

204 $$\varepsilon_{22}=\frac{\partial u_2}{\partial x_2} \tag{3}$$

$$\varepsilon_{12}=\frac{1}{2}\left(\frac{\partial u_1}{\partial x_2}+\frac{\partial u_2}{\partial x_1}\right)=\frac{1}{2}\left(\theta+\frac{\mathrm{d}w_0}{\mathrm{d}x_1}\right)$$

205 For linear elastic materials, the constitutive relationship is:

206 $$\sigma_{ij}=C_{ijkl}\varepsilon_{kl} \tag{4}$$

207 The elasticity tensor C was reduced to that of an isotropic material, yielding the
208 following expressions for the stress components:

$$\sigma_{11}=E\varepsilon_{11}=E\left(\frac{\mathrm{d}u_0}{\mathrm{d}x_1}+x_2\frac{\mathrm{d}\theta}{\mathrm{d}x_1}\right)$$

209 $$\sigma_{12}=2G\varepsilon_{12}=G\gamma_{12}=G\left(\theta+\frac{\mathrm{d}w_0}{\mathrm{d}x_1}\right) \tag{5}$$

210 The resultant force of the cross-section can be obtained through stress integration:

$$N=\int_A\sigma_{11}\mathrm{d}A=E\int_A\left(\frac{\mathrm{d}u_0}{\mathrm{d}x_1}+x_2\frac{\mathrm{d}\theta}{\mathrm{d}x_1}\right)\mathrm{d}A=EA\frac{\mathrm{d}u_0}{\mathrm{d}x_1}$$

211 $$Q=G\int_A\sigma_{12}\mathrm{d}A=G\left(\theta+\frac{\mathrm{d}w_0}{\mathrm{d}x_1}\right) \tag{6}$$

$$M=\int_A x_2\cdot\sigma_{11}\mathrm{d}A=E\int_A\left(x_2\frac{\mathrm{d}u_0}{\mathrm{d}x_1}+x_2^2\frac{\mathrm{d}\theta}{\mathrm{d}x_1}\right)\mathrm{d}A=EI\frac{\mathrm{d}\theta}{\mathrm{d}x_1}$$

212 where N,Q,M represents the axial force, shear force and bending moment on the
213 interface. Study the infinitesimal elements of the beam, Figure 3(c) presents the
214 schematic of the force analysis. The equilibrium equation of this infinitesimal body is
215 expressed as follows:

216 $$\mathrm{d}N+q_1\left(x_1\right)\mathrm{d}x=0 \tag{7}$$

$$\mathrm{d}Q+q_2\left(x_1\right)\mathrm{d}x=0$$

$$\mathrm{d}M-Q\mathrm{d}x+q_1\left(x_1\right)\mathrm{d}x+\frac{1}{2}q_2\left(x_1\right)\mathrm{d}x^2=0$$

217 where, q_1,q_2 represents the complex load under the infinitesimal elements. Ignoring
218 the second-order small quantities, the final control equation is obtained after
219 simplification.:

$$EA\frac{\mathrm{d}^2u_0}{\mathrm{d}x_1^2}+q_1=0$$

$$GA\left(\frac{\mathrm{d}\theta}{\mathrm{d}x_1}+\frac{\mathrm{d}^2w_0}{\mathrm{d}x_1^2}\right)+q_2=0 \tag{8}$$

$$EI\frac{\mathrm{d}^2\theta}{\mathrm{d}x^2}-GA\left(\theta+\frac{\mathrm{d}w_0}{\mathrm{d}x_1}\right)+q_1=0$$

Consider displacement boundary conditions as well as continuity boundary conditions:

$$u(0)=0,\ w(0)=0,\ \theta(0)=0,\ N(L)=0,\ Q(L)=0,\ M(L)=0$$

$$u_L(a)=u_R(a),N_L(a)=N_R(a),\ w_L(a)=w_R(a),Q_L(a)=Q_R(a) \tag{9}$$

$$\theta_L(a)=\theta_R(a),M_L(a)=M_R(a)$$

Where, $u_L, u_R, w_L, w_R, \theta_L, \theta_R, N_L, N_R, Q_L, Q_R, M_L, M_R$ respectively represent the displacements, rotation angles, axial forces, shear forces and bending moments of the left and right sections at the point where the load is applied.

3.2 Stress-strain field model for adhesive joints based on elasticity theory

Problems in elasticity theory are often transformed into boundary value problems involving biharmonic equations. Starting from the three fundamental equations of elasticity theory, their basic form is expressed as：

$$\sigma_{ij,j}=0$$

$$\varepsilon_{ij}=\frac{1}{2}\left(u_{i,j}+u_{j,i}\right) \tag{10}$$

$$\sigma_{ij}=\lambda\varepsilon_{kk}\delta_{ij}+2\mu\varepsilon_{ij}$$

where δ_{ij} represents the Kronecker delta (the component of the unit tensor), ε_{kk}represents the summation convention. According to the balance equation, it can be concluded that the assumed scalar function automatically satisfies. Introduce the Arie stress function $\phi(x_1,x_2)$:

$$\sigma_{11}=\frac{\partial^2\phi}{\partial x_2^2},\ \sigma_{22}=\frac{\partial^2\phi}{\partial x_1^2},\ \sigma_{12}=\frac{\partial^2\phi}{\partial x_1\partial x_2} \tag{11}$$

In the case of planar problems, the strain compatibility equation is obtained by eliminating the displacement through the geometric equation:

$$\frac{\partial\varepsilon_{11}}{\partial x_2^2}+\frac{\partial\varepsilon_{22}}{\partial x_1^2}-\frac{2\partial\varepsilon_{12}}{\partial x_1\partial x_2}=0 \tag{12}$$

Substituting Eqs. (11) into the constitutive equation of Eqs. (10) yields the strain components expressed in terms of the stress function ϕ:

$$\varepsilon_{11}=\frac{1}{E}\left(\frac{\partial^2\phi}{\partial x_2^2}-v\frac{\partial^2\phi}{\partial x_1^2}\right)$$
$$\varepsilon_{22}=\frac{1}{E}\left(\frac{\partial^2\phi}{\partial x_1^2}-v\frac{\partial^2\phi}{\partial x_2^2}\right) \tag{13}$$
$$\varepsilon_{12}=-\frac{2(1+v)}{E}\frac{\partial^2\phi}{\partial x_1\partial x_2}$$

By substituting Eqs. (13) into the strain compatibility Eqs. (12) and simplifying, the biharmonic equation is obtained:

$$\frac{\partial^4\phi}{\partial x_1^4}+2\frac{\partial^4\phi}{\partial x_1^2\partial x_2^2}+\frac{\partial^4\phi}{\partial x_2^4}=0 \tag{14}$$

It can also be expressed as:

$$\nabla^4\phi=0 \tag{15}$$

The boundary conditions are expressed as

$$\begin{aligned}&\sigma_{22}\big|_{x_2=-h}=q_2\ \ (a\le x_1\le L),\ \sigma_{12}\big|_{x_2=-h}=q_1\ \ (a\le x_1\le L)\\&\sigma_{22}\big|_{x_2=h}=0\ \ (a\le x_1\le L),\ \sigma_{12}\big|_{x_2=h}=0\ \ (a\le x_1\le L)\\&\sigma_{22}\big|_{x_2=-h}=0\ \ (0\le x_1\le a),\ \sigma_{12}\big|_{x_2=-h}=0\ \ (0\le x_1\le a)\end{aligned} \tag{16}$$

3.3 Analysis model for stress distribution of joint adhesive layer

Due to the extremely thin thickness of the adhesive layer, it is reasonable to consider the mid-plane stress of the adhesive layer as the load acting on the adherent body. Divide the bonding area into two parts, the upper and the lower (Figure 3(d)), and list the equilibrium equations for each part separately:

$$\begin{aligned}&\frac{dN_1}{dx}+b\tau_a=0,\frac{dN_2}{dx}-b\tau_a=0\\&\frac{dQ_1}{dx}+b\sigma_a=0,\frac{dQ_2}{dx}-b\sigma_a=0\\&\frac{dM_1}{dx}-Q_1+\frac{h_a+h_0}{2}b\tau_a=0,\ \frac{dM_2}{dx}-Q_2+\frac{h_b+h_0}{2}b\tau_a=0\end{aligned} \tag{17}$$

Neglecting shear deformation, the first derivative of the axial displacement (u'_{1a}, u'_{1b}) and the second derivative of the transverse displacement (u_{2a}, u_{2b}) of the differential element can be simplified and expressed as:

$$u_{1a}^{'}=\frac{1}{E_a b h_a}\left(N_1+\frac{6}{h_a}M_1\right),\ u_{1b}^{'}=\frac{1}{E_b b h_b}\left(N_2-\frac{6}{h_b}M_2\right)$$
$$u_{2a}^{''}=-\frac{12}{E_a b h_a^3}M_1,\ u_{2b}^{''}=-\frac{12}{E_b b h_b^3}M_2 \tag{18}$$

Where, E_a and E_b represent the elastic modulus of the upper and lower adhering bodies respectively, h_a and h_b represent the thickness of the upper and lower adhering bodies respectively, and b represents the width of the adhering body. N_1, N_2, Q_1, Q_2, M_1, M_2 respectively represent the axial force, shear force and bending moment on the left and right sides of the bonding area micro-element. The mid-plane shear stress τ_a and peel stress σ_a expressions in the adhesive layer are derived from the deformation compatibility relationships between the upper and lower adherends and the constitutive equations:

$$\tau_a=G_0\frac{u_{1a}-u_{1b}}{h_0},\quad \sigma_a=E_0\frac{u_{2a}-u_{2b}}{h_0} \tag{19}$$

where G_0 is the shear modulus of the adhesive. Taking the second derivative of Eqs (18) with respect to deflection and then subtracting them, substituting the second expression from Eqs. (19) into the result, the following simplified relationship is obtained:

$$u_{2b}^{'''}-u_{2a}^{'''}=-\frac{E_0}{h_0}\left(\frac{12}{E_b h_b^3}+\frac{12}{E_a h_a^3}\right)\left(u_{2b}-u_{2a}\right)-\frac{G_0}{h_0}\left(\frac{6\left(h_b+h_0\right)}{E_b h_b^3}-\frac{6\left(h_a+h_0\right)}{E_a h_a^3}\right)\left(u_{1b}^{'}-u_{1a}^{'}\right) \tag{20}$$

By solving Eqs. (18) for N and M, taking their derivatives, and substituting them into the first expression in Eqs. (17) followed by subtraction, the following equation is obtained:

$$u_{1b}^{''}-u_{1a}^{''}-\frac{h_a}{2}u_{2a}^{''}-\frac{h_b}{2}u_{2b}^{''}-\frac{1}{E_1 h_a}\tau_a-\frac{1}{E_2 h_b}\tau_a=0 \tag{21}$$

Differentiating the equation again and combining it with the first expression in Eqs (8) and with Eq (9) yields the following result:

$$u_{1b}^{'''}-u_{1b}^{'''}+\frac{E_0}{h_0}\left(\frac{6}{E_b h_b^2}-\frac{6}{E_b h_b^2}\right)\left(u_{2b}-u_{2a}\right)-$$
$$\left(\frac{G_0}{h_0}\left(\frac{3(h_b+h_0)}{E_b h_b^2}+\frac{3(h_a+h_0)}{E_a h_a^2}\right)+\frac{1}{E_b h_b}+\frac{1}{E_a h_a}\right)\left(u_{1b}^{'}-u_{1a}^{'}\right)=0 \tag{22}$$

The relationship between the x-direction displacement and the y-direction displacement can be established through Eq (22). Take the derivative of the above

equation and substitute Eq (19) and Eq (20) to obtain the final control equation.

$$\left(u_{2b}-u_{2a}\right)^{(7)}-D_{11}\left(u_{2b}-u_{2a}\right)^{(5)}-A_{11}\left(u_{2b}-u_{2a}\right)''+\left(A_{11}D_{11}+C_{11}B_{11}\right)\left(u_{2b}-u_{2a}\right)'=0 \quad (23)$$

where

$$A_{11}=-\frac{E_0}{h_0}\left(\frac{12}{E_b h_b^3}+\frac{12}{E_a h_a^3}\right), B_{11}=\frac{G_0}{h_0}\left(\frac{6(h_b+h_0)}{E_b h_b^3}-\frac{6(h_a+h_0)}{E_a h_a^3}\right)$$

$$C_{11}=\frac{E_0}{h_0}\left(\frac{6}{E_b h_b^2}-\frac{6}{E_a h_a^2}\right), D_{11}=\frac{G_0}{h_0}\left(\frac{3(h_b+h_0)}{E_b h_b^2}+\frac{3(h_a+h_0)}{E_a h_a^2}\right)+\frac{1}{E_b h_b}+\frac{1}{E_a h_a}$$

This complex differential equation can be solved by the power series method. This approach has also been adopted in previous analytical studies of functionally graded adhesively bonded joints. The assumed solution structure is given by Eq. (24):

$$u_{2b}-u_{2a}=\sum_{i=1}^{7}C_i e^{r_i x} \quad (24)$$

The solution to this equation can be obtained by incorporating the seven boundary conditions:

$$\begin{gathered}\int_{-L}^{L}G_0\frac{u_{1b}-u_{1a}}{h_0}\mathrm{d}x=N_0\\ \left.\frac{\mathrm{d}\left(u_{1b}-u_{1a}\right)}{\mathrm{d}x}\right|_{L}=\frac{1}{E_b b h_b}\left(Q_b+\frac{6}{h_b}M_b\right),\ \left.\frac{\mathrm{d}\left(u_{1b}-u_{1a}\right)}{\mathrm{d}x}\right|_{-L}=-\frac{1}{E_a b h_a}\left(Q_a+\frac{6}{h_b}M_a\right)\\ \left.\frac{\mathrm{d}^2\left(u_{2b}-u_{2a}\right)}{\mathrm{d}x^2}\right|_{L}=\frac{12}{E_b b h_b^3}M_b,\ \left.\frac{\mathrm{d}^2\left(u_{2b}-u_{2a}\right)}{\mathrm{d}x^2}\right|_{-L}=\frac{12}{E_a b h_a^3}M_a\\ \left.\frac{\mathrm{d}^3\left(u_{2b}-u_{2a}\right)}{\mathrm{d}x^3}\right|_{L}=-\frac{12}{E_b b h_b^3}Q_b,\ \left.\frac{\mathrm{d}^3\left(u_{2b}-u_{2a}\right)}{\mathrm{d}x^3}\right|_{-L}=\frac{12}{E_a b h_a^3}Q_a\end{gathered} \quad (25)$$

Within this context, M_a, M_b, Q_a, Q_b denote the bending moments and shear forces at both ends of the bonding region, respectively. Models based on Timoshenko beam theory and two-dimensional elasticity can generally be solved using standard methods under simple loading conditions. However, as shown in Eq. (23), the governing equation in this study is a complex seventh-order differential equation with highly intricate solutions. This complexity renders both the solution of the one-dimensional model and the determination of the stress function in the two-dimensional problem extremely difficult.

4. Construction of the PINNs framework

The rapid growth of computational power has enabled machine learning to revolutionize various research fields by delivering significant improvements in computational efficiency. However, acquiring sufficient data for complex physical

problems remains a significant challenge. A key limitation of conventional architecture such as deep neural networks (DNNs) and convolutional neural networks (CNNs) is their poor stability and convergence when trained on small datasets. This reveals an inherent tension between accuracy and computational efficiency when addressing complex engineering problems. Besides, another major limitation of conventional neural network model is their lack of physical interpretability. To overcome these limitations, embedding physical laws into the loss function guides the neural network toward physically consistent predictions, ensuring robust generalization even with limited training data. In this study, the governing equations of the two investigated theoretical models are inherently difficult to solve analytically or numerically. PINNs offer a powerful and effective alternative for obtaining reliable solutions.

For the Timoshenko beam case described in Section 3.1, the outputs of the finite element model were defined as the axial displacement, transverse displacement, and rotational angle. The adherends were discretized into 60 segments, resulting in a total of 183 output points along the axis. The inputs to the PINNs consisted of four geometric parameters of the joint: the thicknesses of the upper and lower adherends, the adhesive layer thickness, and the bond length. Using Latin Hypercube Sampling (LHS), 50 combinations of input parameters were generated within the predefined variable ranges. Each combination was then evaluated through finite element analysis to obtain the corresponding output responses. The resulting input-output pairs formed the dataset for subsequent machine learning model training. The four input parameters were defined as follows: half the bond overlap length ($l/2$), half the adhesive layer thickness ($h_a/2$), the thickness of the top adherend (h_1), and the thickness of the bottom adherend (h_2). The specific ranges of these parameters are provided in Table 3.

Table 3. The range of input parameters for PINNs.

Parameters (LHS)	Lower bound	Upper bound	Symbol
Half of Bond overlap length $l/2$ (mm)	20	25	P1
Half of Thickness of adhesive $h_a/2$ (mm)	0.2	0.5	P2
Thickness of top adherend h_1 (mm)	4	8	P3
Thickness of bottom adherend h_2 (mm)	4	8	P4

Within the PINNs framework, the input data were first normalized to a uniform scale to eliminate the effects of different dimensions and ranges, thereby improving the convergence rate. The network architecture consisted of an input layer with four neurons corresponding to the four geometric parameters, an output layer with 183

neurons, and five hidden layers each containing 500 neurons. The hyperbolic tangent (tanh) was adopted as the activation function, and an early stopping mechanism was employed during training. Five-fold cross-validation was performed to ensure model generalizability, and the optimal model was selected to predict the output responses for new geometric configurations. The total loss was defined as a weighted combination of the data loss and the physical loss, with the latter derived from the governing equations Eq. [8] and Eq. [15], and boundary conditions Eq. [9] and Eq. [25] described in Section 3.1. The weighting coefficients were set to 0.2 for the data loss and 0.8 for the physical loss. The calculation formulas for data loss and physical loss are as follows:

$$\begin{aligned} \mathrm{L}_{data} &= \frac{1}{N}\sum_{i=1}^{N} \| \ \hat{Y}_i - Y_i \|^2 \\ \mathrm{L}_{physics} &= \frac{1}{N}\sum_{i=1}^{N}\left(\left\| f_{eq}\left(x_i, y_i\right)\right\|^2 + \left\| f_{bc}\left(x_i, y_i\right)\right\|^2 \right) \end{aligned} \tag{26}$$

Where, $\mathcal{L}_{data}$ indicates data loss, $\hat{Y}_i$ is predicted value and Y_i is true values, N denotes the number of evaluation points used to compute each loss term; $\mathcal{L}_{physics}$ indicates physics loss, f_{eq} and f_{bc} respectively represent the residuals of the partial differential equation and the boundary condition constraints.

For the stress-strain field problem of the elasticity model described in Section 3.2, the output was extended from one dimension to two dimensions. The adherends were discretized into nine layers. This discretization balanced computational efficiency with the accuracy of numerical differentiation and resulted in each stress component being represented as a 9×61 matrix. The training data accordingly comprised three stress component matrices: σ_{11}, σ_{22}, and σ_{12}. The spatial coordinates of the grid were generated, and the number of neurons in the output layer of the neural network was correspondingly modified to 1647 to accommodate the increased dimensionality. Accordingly, the governing equation in the physical loss term was modified to the biharmonic equation, and the boundary conditions were updated to reflect stress boundary conditions. The detailed architecture of the PINNs is illustrated in Figure 4.

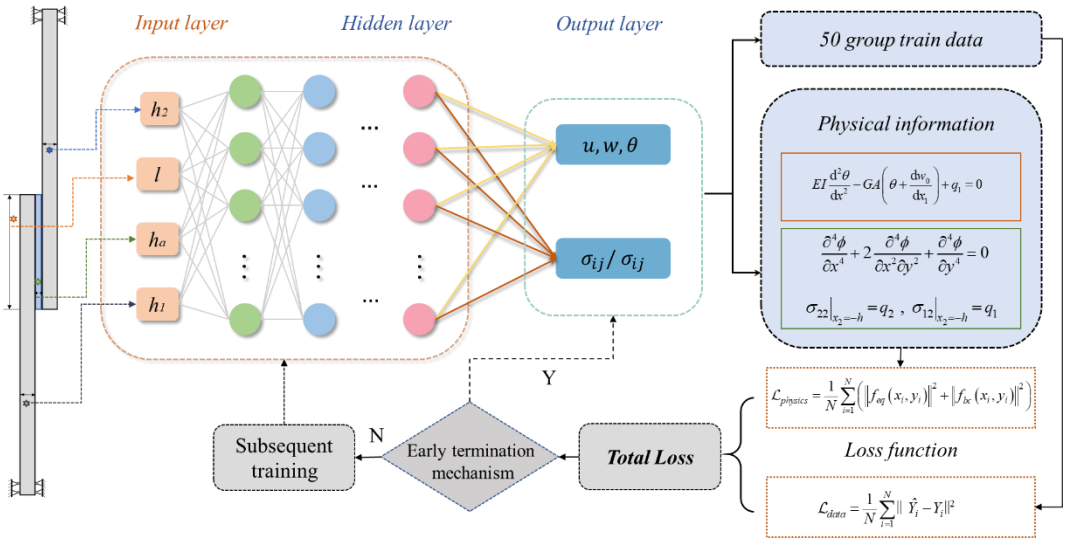

Figure 4. Schematic diagram of the principle of the PINNs framework.

5. Results and Discussions

5.1. Verification of the finite element model

Figure 5 presents a comparison between the experimental and finite element results for the two bonding configurations: Al-CFRP and CFRP-CFRP, each with five replicate tests. Prior to joint failure, good agreement was observed in terms of stiffness. While the finite element model was developed under idealized conditions, minor defects were inevitably introduced during specimen fabrication. This led to slight discrepancies between the numerical and experimental results; however, the deviations remained within an acceptable range. For the Al-CFRP joints, the failure loads obtained from both experiments and finite element simulations ranged from 16 kN to 18 kN, with corresponding displacements at failure between 1.0 mm and 1.2 mm. In the case of CFRP-CFRP joints, failure loads were maintained at 16 kN to 18 kN while achieving a significant weight reduction. The failure displacements, however, exhibited a broader range of 1.0 to 1.4 mm, reflecting the slightly lower elastic modulus of CFRP relative to aluminum.

The close agreement between the experimental and finite element results for both failure load and displacement at failure, across the two bonding configurations, demonstrates the accuracy of the developed finite element model. The failure modes of the bonded joints are illustrated in Figure 1(b). For the asymmetric Al-CFRP configuration, differential deformation between the upper and lower adherends led to cohesive fracture initiating within the adhesive layer. In contrast, the CFRP-CFRP joints exhibited adhesive failure, characterized by complete detachment of the adhesive layer from one adherend surface.

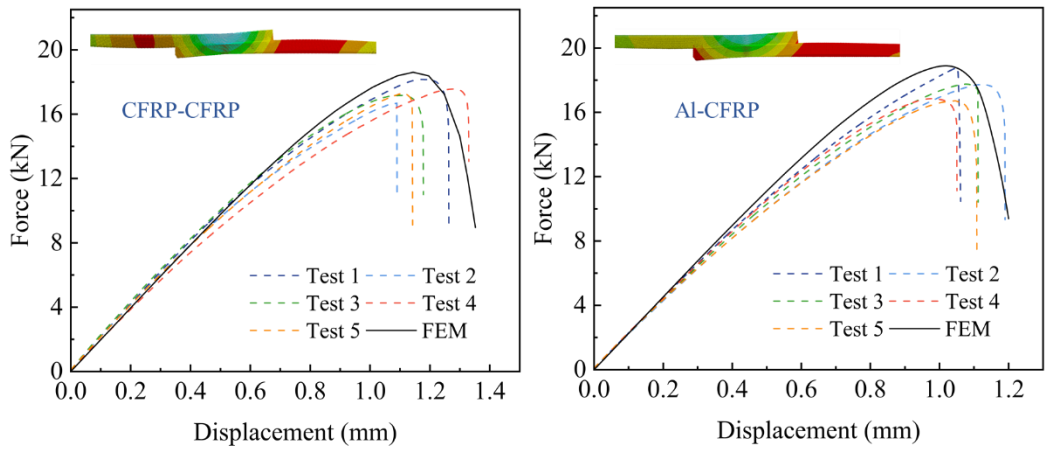

Figure 5. Comparison of the force-displacement curve results between the finite element model and the experiment (a) CFRP-CFRP, (b) Al-CFRP.

5.2. Verification of the one-dimensional PINNs

Figure 6 validates the accuracy of the one-dimensional PINNs framework for both bonding configurations. Following the five-fold cross-validation scheme described earlier, the training set comprised 40 samples and the test set 10 samples. For each sample, the axial displacement u and transverse displacement (deflection) w were predicted. The R^2 curves in the figure were obtained by calculating the correlation between the predicted and true values for each sample. For the CFRP-CFRP configuration, the R^2 values for axial displacement predictions remained above 0.995 across all training samples. Regarding transverse deflection, the vast majority of training samples also achieved R^2 values exceeding 0.995, with only one sample falling slightly below this threshold—though still above 0.990. The test set results likewise exhibited strong correlations between predictions and ground truth. For the Al-CFRP configuration, the asymmetric nature of the joint increased the prediction difficulty. A further underlying reason can be traced to the modeling approach adopted in this study: the stresses at the mid-plane of the adhesive layer are equivalently represented as distributed loads on the bonding surface. Under asymmetric configurations, this equivalent representation may introduce slight inaccuracies, which contribute to the increased prediction errors. Nevertheless, the correlations for both training and test sets remained around 0.95. These results demonstrate the satisfactory predictive accuracy of the one-dimensional PINNs model.

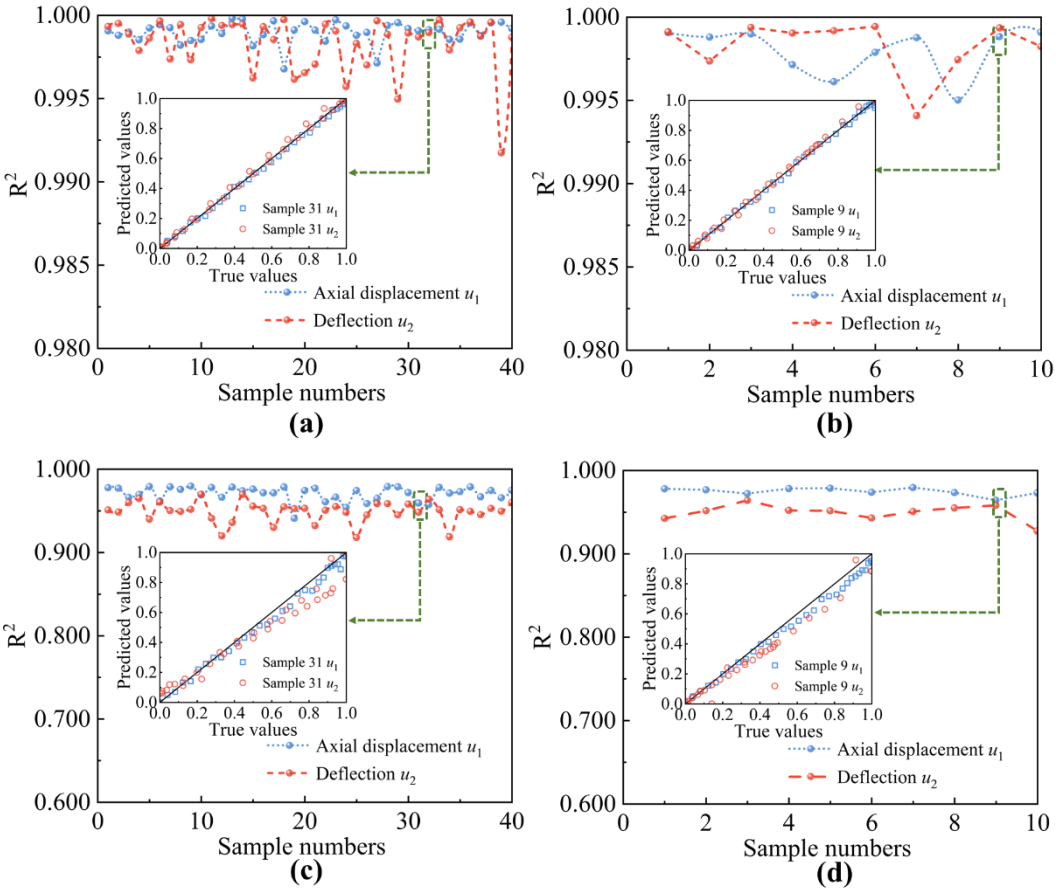

Figure 6. Accuracy verification of the one-dimensional PINNs framework for the bonded joint (a) CFRP-CFRP train group, (b) CFRP-CFRP test group, (c) Al-CFRP train group, (b) Al-CFRP test group.

Furthermore, the results of the sensitivity analysis on the weighting between the physical loss and the data loss are presented in Table 4, where the R^2 values for both the training and test sets are listed for different joint configurations under various weighting ratios. “DNN” refers to a deep neural network without any physical information. As the weight of the physical loss increases, the R^2 values exhibit a trend of first rising and then declining, indicating that the 0.8/0.2 ratio yields the best accuracy and generalization of the framework. When the ratio is set to 0.9/0.1, a decline in R^2 is observed, which can likely be attributed to the data loss weight being too low for the PINN framework to capture the fundamental data trends. For the DNN without physical constraints, 50 data samples are insufficient to capture such complex behavior. This contrast highlights a key advantage of the PINN framework over purely data-driven networks, namely the ability to make accurate predictions even with limited data.

Table 4. Sensitivity Analysis Results of physical information and data weights.

Average R^2	0.7/0.3	0.8/0.2	0.9/0.1	DNN
CFRP-CFRP train *u*	0.9474	0.9989	0.9988	0.8243
CFRP-CFRP train *w*	0.8294	0.9983	0.8954	0.7496
CFRP-CFRP test *u*	0.9344	0.9979	0.9849	0.8335
CFRP-CFRP test *w*	0.8269	0.9987	0.9037	0.7343
Al-CFRP train *u*	0.8272	0.9708	0.9883	0.7843
Al-CFRP train *w*	0.7878	0.9493	0.8906	0.7072
Al-CFRP test *u*	0.8945	0.9748	0.9770	0.7162
Al-CFRP test *w*	0.7952	0.9496	0.8851	0.7114

5.3. Prediction of adherends deformation using the one-dimensional PINNs

Figure 7 presents a comparison of the deformation predictions from the one-dimensional PINNs framework and the finite element model for CFRP-CFRP bonded joints with three different adherend thicknesses. For the x-direction displacement (Figure 7(a) and 7(b)), the results obtained with upper and lower adherend thicknesses of 5 mm-5 mm closely resembled those with 5 mm-8 mm, both yielding displacements of approximately 0.08 mm. The case with a bond length of 40 mm produced slightly higher displacements than that with 50 mm. This indicates that longer bond lengths result in smaller axial displacements under the same loading conditions. Furthermore, the thickness of the lower adherend does not significantly influence the x-direction displacement of the upper adherend. Regarding the y-direction displacement (deflection) (Figure 7(c) and 7(d)), the overall trend exhibits a negative-to-positive pattern, which arises from the rotation of the bonded region under eccentric loading. For the 5 mm-5 mm adherend configuration, the minimum deflection reaches approximately -0.2 mm. In the 8 mm-8 mm case, the minimum deflection decreases to -0.1 mm, while for the asymmetric 5 mm-8 mm configuration, it further drops to -0.4 mm. Additionally, it is observed that the minimum deflection point for the bond length of 40 mm is located slightly to the right of that for the 50 mm bond length.

The results for the Al-CFRP structure are shown in Figure 8, the overall results do not deviate substantially from those of the CFRP-CFRP joints. The x-direction displacements (Figure 8(a) and 8(b)) are slightly smaller than those of the symmetric configuration, which can be attributed to the higher elastic modulus of aluminum. Regarding the y-direction displacement ((Figure 8(c) and 8(d))), some fluctuations are observed near the point of load application. Nevertheless, the peak values and overall

trends remain in good agreement. In summary, the one-dimensional PINNs framework based on Timoshenko beam theory demonstrates satisfactory predictive accuracy. Furthermore, it was observed that in the asymmetric bonding configuration with an upper adherend thickness of 5 mm and a lower adherend thickness of 8 mm, the deflection was even greater than that of the symmetric 5 mm-5 mm case. This can be attributed to the greater thickness of the lower adherend, and hence its higher stiffness, which caused the majority of the deformation to be concentrated in the thinner 5 mm upper adherend under loading.

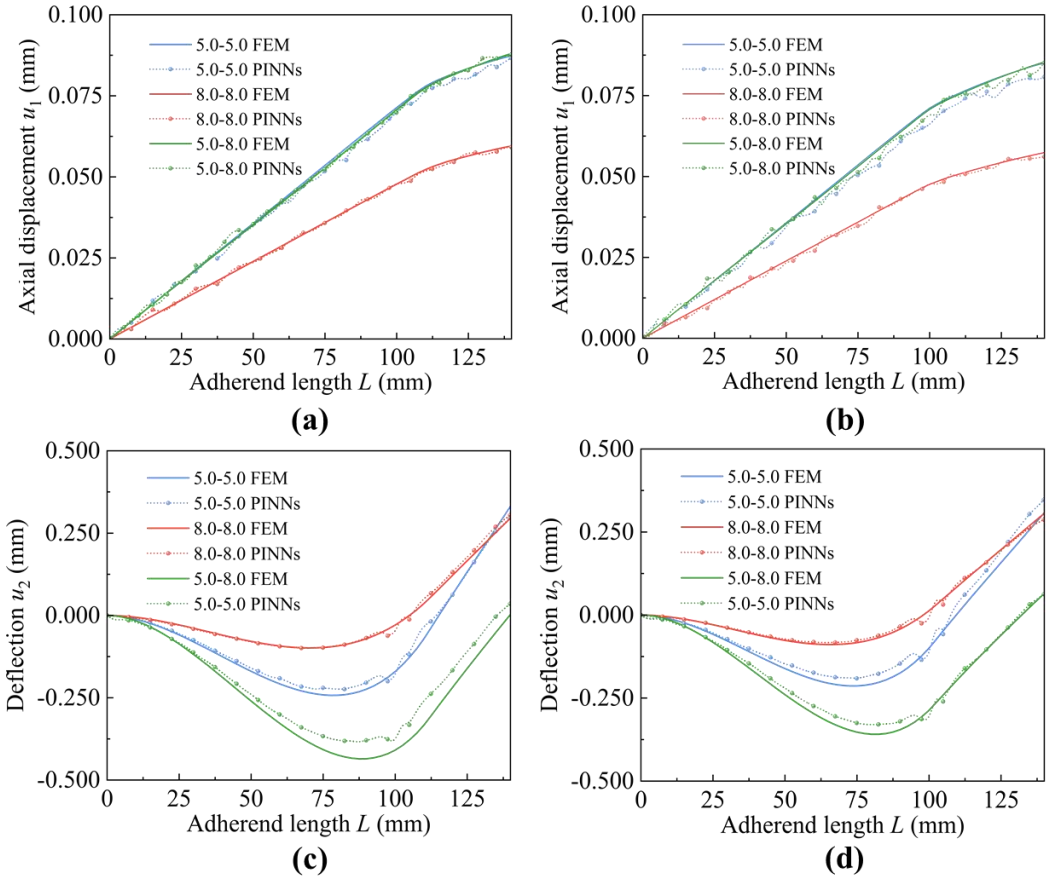

Figure 7 Comparisons of predicted adherend deformations for CFRP-CFRP lap joints with bonding lengths of (a) 40mm and (b) 50mm of u_1; (c) 40mm and (d) 50mm of u_2.

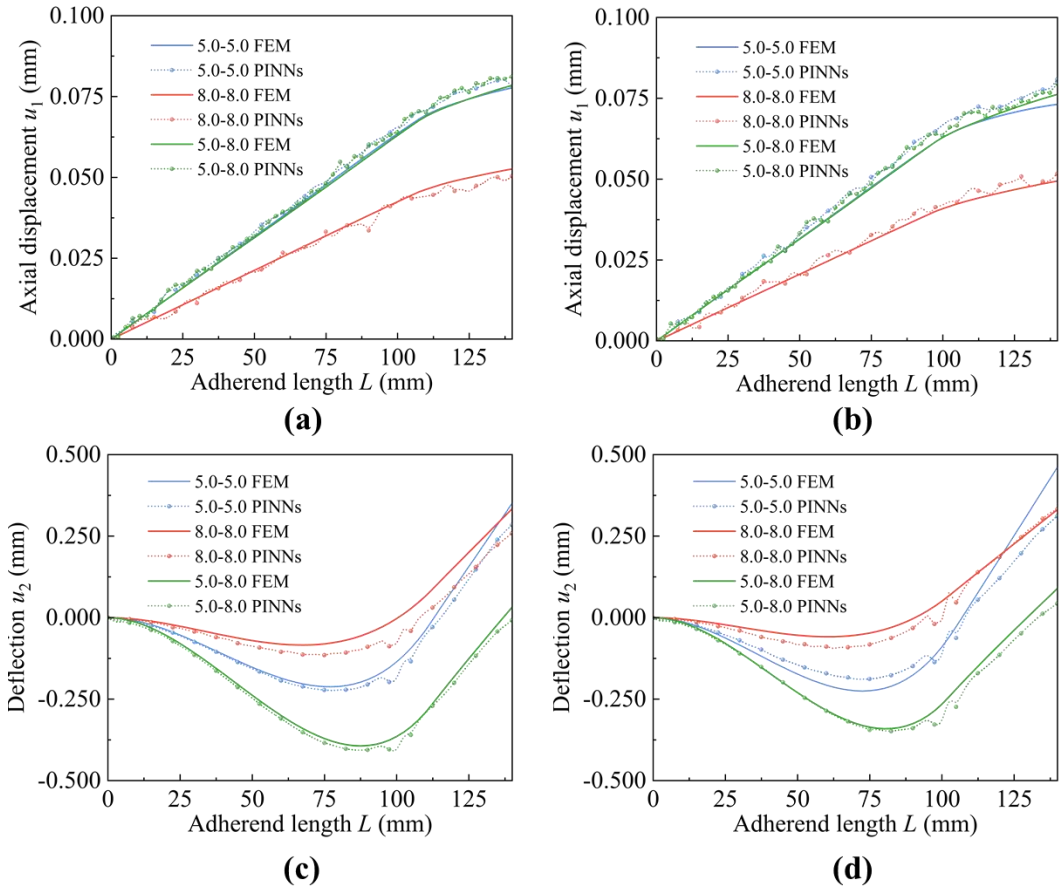

Figure 8. Comparisons of predicted adherend deformations for Al-CFRP lap joints with bonding lengths of (a) 40mm and (b) 50mm of u_1; (c) 40mm and (d) 50mm of u_2.

5.4. Verification of the two-dimensional PINNs

Figure 9 demonstrates the accuracy of the two-dimensional PINNs framework by comparing the predicted and true values of the stress components (σ_{11}, σ_{22}, and σ_{12}) within the adherends for both training and test sets. For the normal stress σ_{11} (Figure 9(a) and 9(b)), with the insets showing detailed predictions versus true values for representative samples. Due to the presence of abrupt changes in the stress distribution, the results were not normalized, the correlation coefficient R^2 was calculated directly from the actual values.

For the CFRP-CFRP bonded joints, both the training set (40 samples) and test set (10 samples) achieved R^2 values exceeding 0.95 for σ_{11} predictions. The highest R^2 in the training set was 0.980 (31st sample), while the test set reached a maximum of 0.973 (5th sample). For the Al-CFRP configuration, approximately three-quarters of the training samples achieved R^2 values above 0.95, while the remaining nine samples,

484 though slightly below this threshold, still exceeded 0.90. The test set results were
485 similarly robust, with the majority above 0.95 and only a few marginally lower, yet
486 consistently above 0.90. This performance degradation is attributed to the asymmetric
487 nature of the Al-CFRP joint, which substantially increases the difficulty of model
488 training.
489 Figure 9(c) and 9(d) illustrate the distribution of the transverse normal stress σ_{22}
490 for the two bonding configurations. The degree of nonlinearity in σ_{22} is considerably
491 higher than that observed for σ_{11}, as evident from the insets. Specifically, σ_{11} exhibits
492 relatively uniform distribution across the domain, whereas σ_{22} is concentrated within
493 a localized region, precisely the area near the bond-line edge where stress concentration
494 occurs. Moreover, σ_{22} is highly sensitive to geometric parameters, particularly the
495 adhesive layer thickness, which further complicates prediction and leads to slightly
496 reduced correlations and increased volatility. For CFRP-CFRP joints, the training set
497 R^2 values for σ_{22} consistently fluctuated above 0.90, with only one test sample falling
498 below this threshold. For Al-CFRP joints, greater fluctuations were observed; although
499 a small portion of samples exhibited correlations below 0.90, they remained within an
500 acceptable range.
501 Figure 9(e) and 9(f) present the results for the shear stress σ_{12}. Consistent with the
502 observations above, the correlations for Al-CFRP joints were slightly lower than those
503 for CFRP-CFRP joints. In the training set, the maximum R^2 for CFRP-CFRP reached
504 0.99, whereas the highest value for Al-CFRP was only 0.902. The test set results
505 exhibited a similar trend.

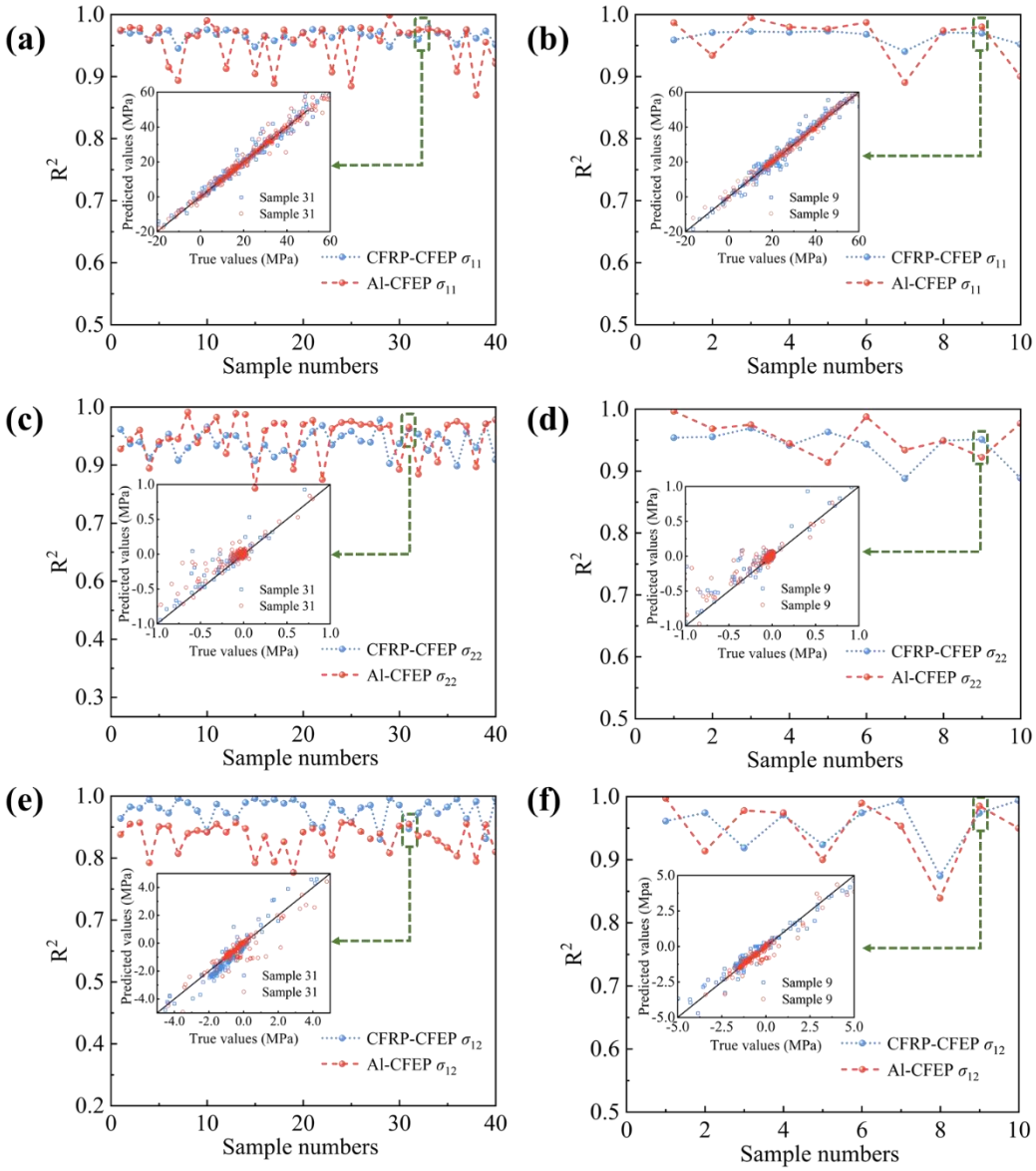

Figure 9. Accuracy verification of the two-dimensional PINNs framework for the bonded joint: (a) σ_{11}, (c) σ_{22}, and (e) σ_{12} for the training group; (b) σ_{11}, (d) σ_{22}, and (f) σ_{12} for the testing group.

5.5. Prediction of adherend stress distributions using the two-dimensional PINNs

The two-dimensional PINNs framework was employed to predict stress distribution for the new dimensions, and a comparison was made with the FE results (Figure 10).

For the σ_{11} distribution (Figure 10(a) and 10(d)), the maximum and minimum values were 145.5 MPa and -18 MPa, respectively. Within the longitudinal range of 0-40 mm, the adherend was predominantly in a tensile state. In addition, the degree of tension on the upper surface exceeded that on the lower surface. This can be attributed to the eccentric loading, which induced downward deformation of the adherend near the fixed end. In the 80-100 mm range, the stress distribution exhibited a pattern where

519 the lower portion was in tension while the upper portion was in compression, resulting
520 from the additional bending moment generated in the bonded joint under load. Beyond
521 100 mm, the stress values approached zero, as the adhesive layer constrained further
522 deformation of the adherend. Furthermore, on the left side of the bonding area on the
523 lower surface, a stress concentration phenomenon occurs.
524 For the σ_{22} distribution (Figure 10(b) and 10(e)), the maximum and minimum
525 values were 80 MPa and -20 MPa, respectively. The stress remained near zero across
526 most of the domain, with pronounced peaks observed only on both sides of the bond-
527 line region on the lower surface. Due to material continuity, the stress gradually
528 decreased from the lower to the upper surface, eventually diminishing to zero at the top
529 surface.
530 For the distribution of shear stress σ_{12} (Figure 10(c) and 10(f)), the maximum and
531 minimum values were 15 MPa and -40 MPa, respectively. Similar to σ_{22}, the shear
532 stress approached zero across most of the domain, with pronounced peaks appearing on
533 both sides of the bond-line region on the lower surface. Notably, a region of positive
534 shear stress emerged in the intermediate zone along the y-direction. This can be
535 attributed to the rotation of the bonded region under tensile loading, which induced a
536 force component perpendicular to the adhesive layer near the bond edges. Consequently,
537 this portion of the adherend experienced tension not only in the x-direction but also in
538 the y-direction, giving rise to the observed shear stress. The principal stress contours
539 (Figure 10(d) and 10(h)) also exhibit strong consistency, and their patterns closely
540 resemble those of σ_{11}, indicating that σ_{11} dominates the tensile response of the bonded
541 joint. This observation further supports, from an additional perspective, the validity of
542 the isotropic simplification adopted in this study.
543 The total loss remained consistently below 0.1 throughout the training process.
544 Although a sudden spike occurred at around 5500 epochs, it rapidly returned to a very
545 low value. The sudden change in the loss can be attributed to the global search behavior
546 of the training process. The PINNs framework begins searching for an optimal solution
547 from a given set of initial parameters. After the training reaches a certain stage, the
548 initial values are reset and training restarts, which causes a sudden jump in the loss.
549 This does not compromise the accuracy of the results. Among the loss components,
550 physical loss was the lowest, indicating that the trained model successfully captured the
551 underlying physical laws.
552

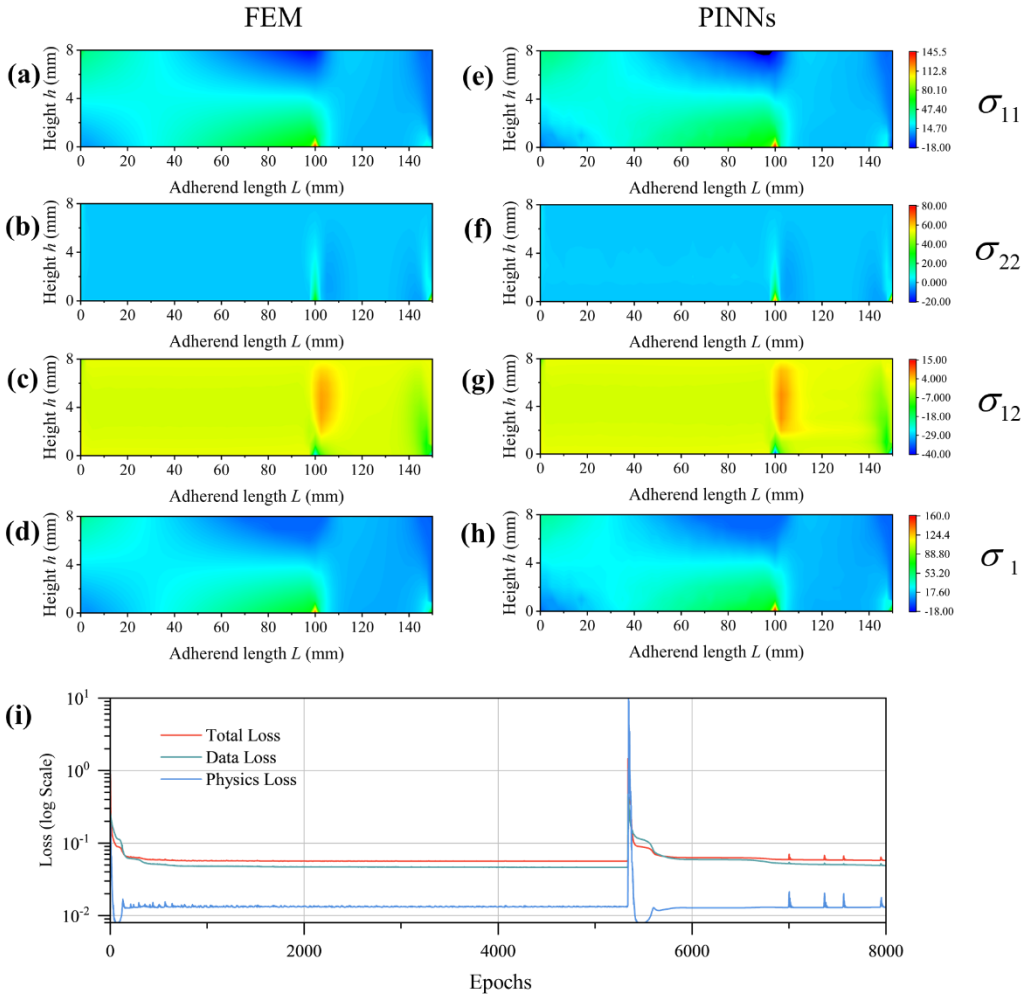

Figure 10. CFRP-CFRP lap joint stress contour map comparison and loss curve (a) σ_{11}, (b) σ_{22}, (c) σ_{12}, and (d) σ_1, by FEM, and (e) σ_{11}, (f) σ_{22}, (g) σ_{12}, and (h) σ_1 by PINNs, with their corresponding (i) loss curves.

Figure 11 presents the stress distributions on the upper and lower surfaces of the adherend for the CFRP-CFRP bonded joint. For the normal stress σ_{11} (Figure 11(a) and 11(e)), the upper surface exhibits a decreasing-increasing-decreasing pattern along the bond line, with a maximum of approximately 50 MPa and a minimum of -20 MPa. This trend aligns with the geometric deformation behavior discussed in Section 5.3. On the lower surface, σ_{11} reaches a peak of approximately 150 MPa, with a minimum of 0 MPa, indicating that the lower surface is entirely in a tensile state. Regarding the transverse normal stress σ_{22} (Figure 11(b) and 11(f)), the maximum on the lower surface is 60 MPa, while the minimum is -5 MPa. Notably, the stress on the upper surface is zero except near the fixed end, and on the lower surface, it vanishes outside the bonded region. This localization of stress is consistent with the Saint-Venant principle in elasticity. The shear stress σ_{12} (Figure 11(c) and 11(g)) exhibits an analogous pattern, with a peak value of -40 MPa on the lower surface. Overall, both the

trend of the results and the size at the peak points show a high degree of consistency Based on the foregoing analysis and the stress contour maps. Furthermore, specific computational times were evaluated to quantify the efficiency improvement of the PINN framework over the finite element model. The finite element simulation required 767 s, whereas the PINN framework completed both training and prediction in only 473 s, achieving a 38.3% reduction in computation time. This advantage becomes even more pronounced when the time spent on mesh generation is also considered.

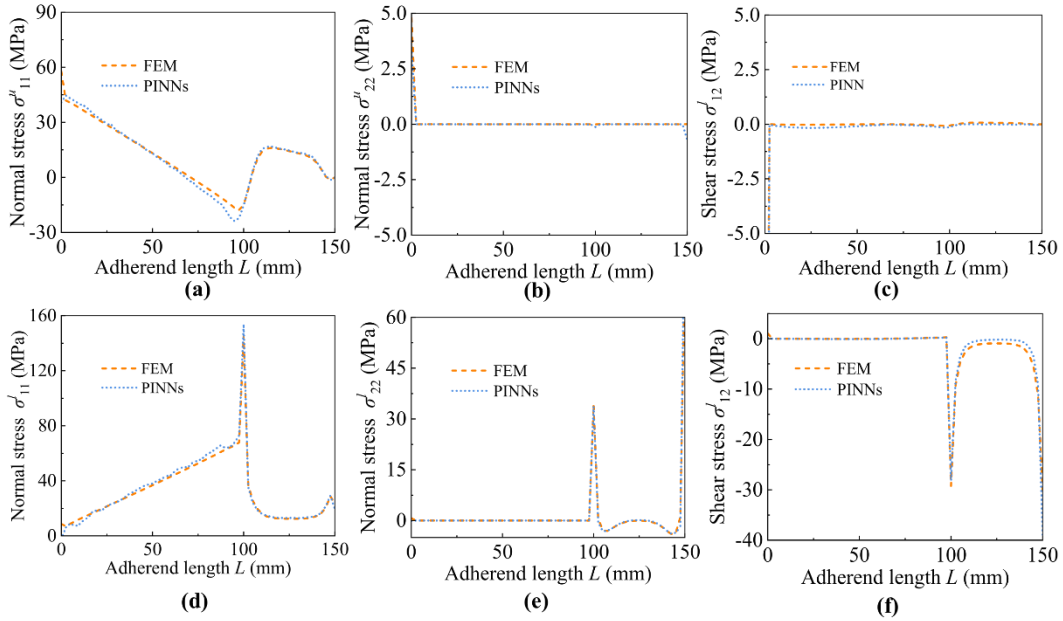

Figure 11. Stress distribution curves of the bonded surfaces of CFRP-CFRP lap joints. (a) σ^u_{11}, (b) σ^u_{22}, and (c) σ^u_{12} of the upper surface, and (d) σ^l_{11}, (e) σ^l_{22}, and (f) σ^l_{12} of the lower surface.

The non-joined stacking result is shown in Figure 12. Compared with the symmetric CFRP-CFRP configuration, the Al-CFRP joint presents greater prediction challenges due to its non-uniform stress and deformation distributions. The general pattern of the results remains similar to that of the symmetric lap joint, with the primary differences lying in the numerical values. For the σ_{11} distribution (Figure 12 (a) and 12(b)), the maximum and minimum values are 120 MPa and -30 MPa, respectively. The PINNs framework underestimates the peak stress at the edge of the bonding area on the lower surface, while slightly overestimating the stress on the upper region of the same surface. Regarding σ_{22} (Figure 12 (c) and 12(d)), the upper and lower limits are consistent with those of the symmetric CFRP-CFRP joint. Due to the slightly lower elastic modulus of CFRP compared to Al, the shear stress result of the Al-CFRP lap joint is less than that of the CFRP-CFRP lap joint. There is only a slight difference between the shear stress (Figure 12 (e) and 12(f)) result and the symmetrical result. Notably, in the intermediate region where the predicted shear stress values are positive,

the PINNs results are slightly higher than those obtained from the finite element model. This minor discrepancy can be attributed to the inherent difficulty of the PINNs framework in accurately capturing the behavior of asymmetric bonded structures. Furthermore, the principal stress contours show relatively high values over the range of approximately 60–110 mm along the horizontal coordinate. This provides practical guidance for engineering applications: inspections should not focus solely on the bond edges but be extended to cover a broader area accordingly.

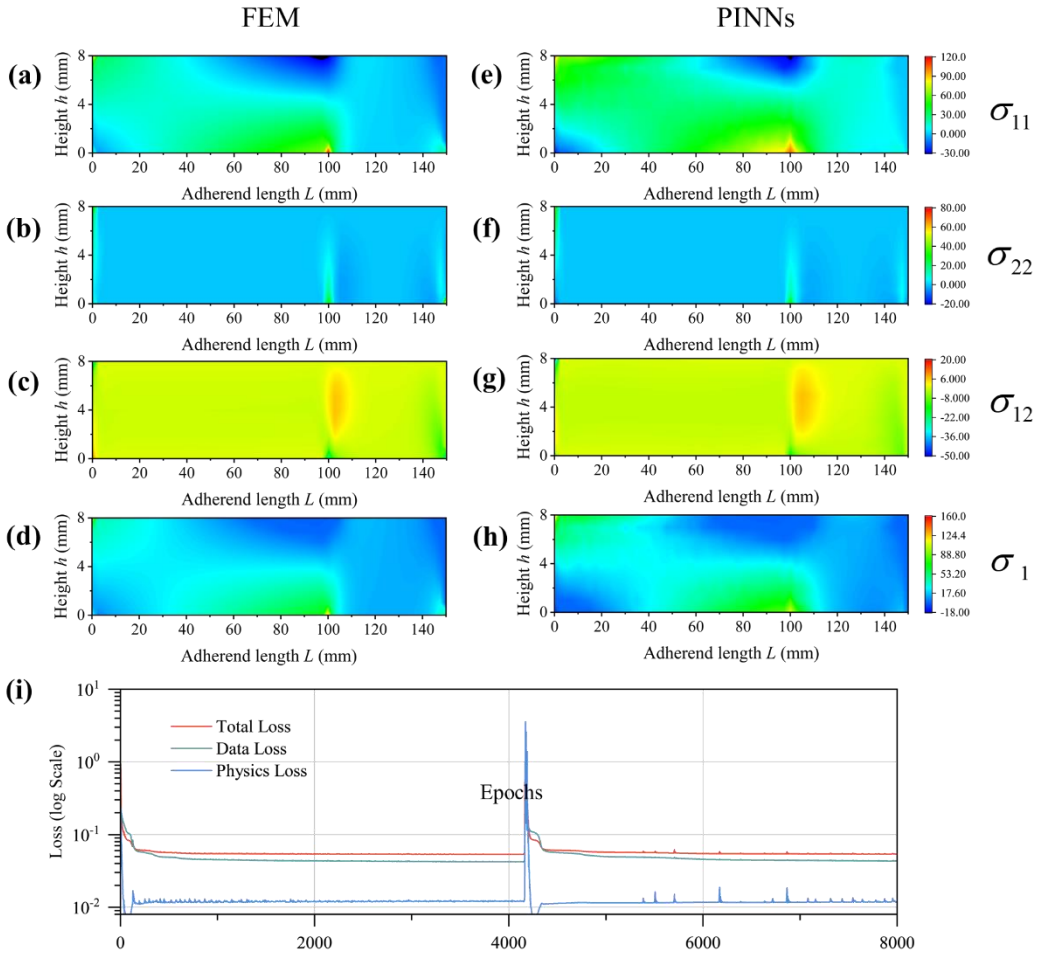

Figure 12. Al-CFRP lap joint stress contour map comparison and loss curve (a) σ_{11}, (b) σ_{22}, (c) σ_{12}, and (d) σ_1, by FEM, and (e) σ_{11}, (f) σ_{22}, (g) σ_{12}, and (h) σ_1 by PINNs, with their corresponding (i) loss curves.

The stress distributions on the upper and lower surfaces of the Al-CFRP joint are presented in Figure 13. The overall pattern follows the same characteristics observed in the symmetric CFRP-CFRP configuration discussed above. For the normal stress σ_{11} (Figure 13(a) and 13(d)) on the upper surface, the difference between the two configurations is negligible. On the lower surface, however, the σ_{11} values predicted by the PINNs framework are slightly lower than those obtained from the finite element

model. Regarding σ_{22} (Figure 13(b) and 13(e)), the finite element results show a value of approximately 37 MPa on the left side of the bonding area, whereas the PINNs predictions are marginally higher, reaching 40 MPa. For the shear stress σ_{12} (Figure 13(c) and 13(f)), the PINNs framework yields values approximately 4 MPa higher than those of the symmetric joint on the left side of the bonding area. Although minor discrepancies between the PINNs framework and the finite element model exist at peak values, all of which remain within an acceptable range, the overall stress distributions show strong consistency. Based on the foregoing analysis and the stress contour maps, it can be concluded that the PINNs framework demonstrates accurate predictive capability for Al-CFRP bonded joints.

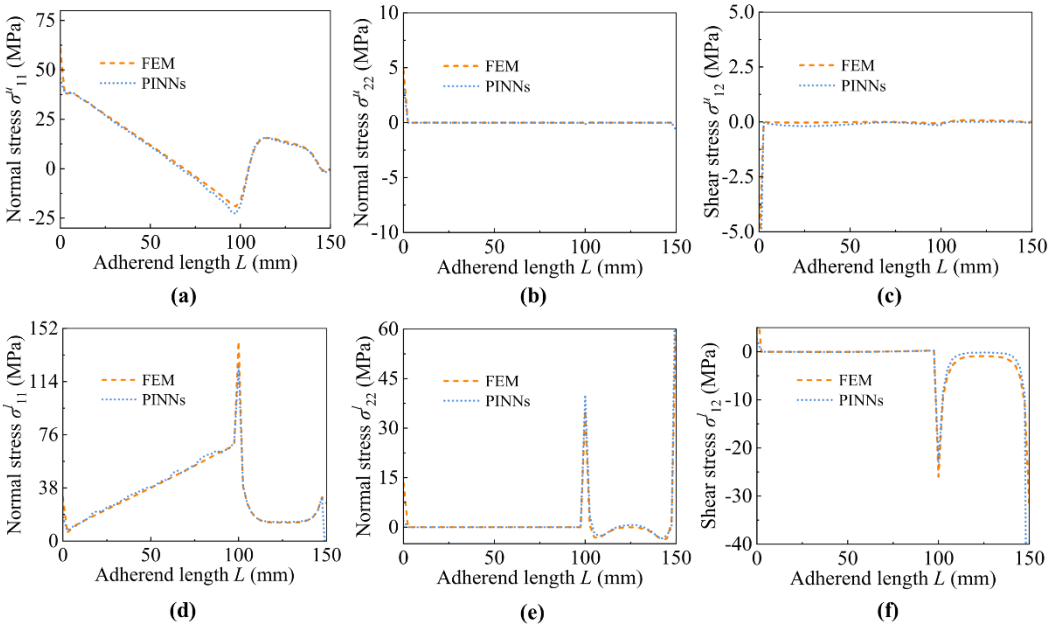

Figure 13. Stress distribution curves of the bonded surfaces of Al-CFRP lap joints. (a) σ^u_{11}, (b) σ^u_{22}, and (c) σ^u_{12} of the upper surface, and (d) σ^l_{11}, (e) σ^l_{22}, and (f) σ^l_{12} of the lower surface.

In addition, as shown in Table 5, the normalized mean absolute errors (NMAE) of the displacement and stress components predicted by the two PINN frameworks are presented. Because the different stress components and displacements span different orders of magnitude, directly comparing their absolute MAE values can be misleading: even when the relative errors are similar, quantities with larger magnitudes naturally produce larger MAE values. For the CFRP-CFRP configuration, the NMAE values are all below 0.12. with the displacement u_1 achieving an exceptionally low value of 0.0298, while the transverse displacement u_2 yields a value of 0.0895 and the normal stress $\boldsymbol{\sigma_{11}}$ at 0.1104. The peel stress $\boldsymbol{\sigma_{22}}$ and shear stress $\boldsymbol{\sigma_{12}}$show NMAE values of 0.0779 and 0.0667, respectively. For the asymmetric Al-CFRP configuration, the errors increase moderately, as expected due to the greater mechanical complexity. Nevertheless, the NMAE for $u_1$remains only 0.0434, and u_2 increases modestly to

0.1052. The stress component errors stay within a narrow range (0.0793 to 0.1233), which are all well below conservative tolerance levels. These normalized error metrics demonstrate that both PINN frameworks yield satisfactory overall accuracy across different joint configurations. The model's ability to maintain consistently acceptable NMAE values despite the transition from symmetric to asymmetric configurations, and across displacement and stress fields of varying magnitudes, underscores its sufficient precision and robust generalization capability.

Table 5. Normalized MAE of the results for the two PINNs frameworks.

	u_1	u_2	σ_{11}	σ_{22}	σ_{12}
CFRP-CFRP	0.0298	0.0895	0.1104	0.0779	0.0667
Al-CFRP	0.0434	0.1052	0.1233	0.0872	0.0793

6. Conclusion

This study employed a combined approach of experimental testing, finite element simulation, theoretical analysis, and PINNs to investigate the deformation and stress distribution in adhesive joints. Two joint configurations were examined: symmetric CFRP-CFRP and hybrid Al-CFRP. The main findings and contributions are summarized as follows:

Based on the Timoshenko beam theory and elasticity theory, the governing equations for the bonded joint under eccentric loading were derived, along with those governing the stress distribution within the adhesive layer. Applying the adhesive layer stress as a load to the adherend makes it exceedingly difficult to solve the one-dimensional model or to assume an appropriate stress function for the two-dimensional problem, owing to the extreme complexity of the solution.

Five sets of tensile tests were conducted on two types of bonded composite joints (CFRP-CFRP and Al-CFRP). The established finite element model demonstrated good agreement with the experimental force-displacement responses. Furthermore, the experimental results reveal that the asymmetric deformation in Al-CFRP joints leads to cohesive failure within the adhesive layer, whereas CFRP-CFRP joints exhibit adhesive failure characterized by peeling. The underlying mechanisms governing these distinct failure modes warrant further detailed investigation. Based on the experimental data and simulation results, One-dimensional and two-dimensional PINNs were established to predict the mechanical response of adhesive joints. The physical loss functions were constructed using the displacement governing equation along with displacement and continuity boundary conditions for the one-dimensional model, and the biharmonic equation with stress boundary conditions for the two-dimensional model. Both PINNs

frameworks achieved a high level of predictive accuracy, with R^2 values consistently exceeding 0.9.

Employing the trained PINNs frameworks, the displacement and stress distributions of the adherends were predicted. The displacements obtained from the one-dimensional PINNs achieved errors below 0.1 mm. For the two-dimensional PINNs, the stress errors, as reflected in the stress distribution curves on the upper and lower surfaces, remained within 5 MPa. Overall, both PINNs frameworks maintained exceptionally high prediction accuracy for new geometric dimensions.

In sum, the proposed PINNs framework overcomes the limitations of existing theoretical models by effectively accounting for complex geometries and material parameters. It provides a fast and efficient approach for predicting the strength of adhesive joints and serves as a versatile framework for solving complex partial differential equations in other engineering applications. Nevertheless, the method has certain limitations. First, the current predictions are limited to interpolation scenarios within the trained parameter ranges; the model's performance under extrapolation to geometries beyond these ranges has not been validated and warrants caution. Second, the model adopts an isotropic simplification for the adherends, which may not be applicable to other joint configurations, and the theoretical framework for the adhesive joint does not incorporate failure criteria. Addressing these limitations will be a key focus of our future work. In summary, this work provides a powerful tool for accurate strength prediction and design optimization of adhesive joints.

Acknowledgement

This work is funded by the Shandong Provincial Excellent Young Scientists Fund (Grant No.: 2024HWYQ-049), the National Natural Science Foundation of China (Grant No.: 12402109), and the National Natural Science Foundation of China (Grant No. 52305336).

Reference

[1] N. Hu, L. Shu, X. Zheng, Z. Deng, X. Cang, A review of modification methods, joints and self-healing methods of adhesive for aerospace, Sci Prog, 107 (2024) 368504241242271. http://dx.doi.org/10.1177/00368504241242271

[2] Y. Wei, X. Jin, Q. Luo, Q. Li, G. Sun, Adhesively bonded joints - A review on design, manufacturing, experiments, modeling and challenges, Composites Part B: Engineering, 276 (2024) 111225. https://doi.org/10.1016/j.compositesb.2024.111225

[3] P. Nunes, E. Marques, A. Akhavan-Safar, C. Borges, R. Carbas, L.F.M. Silva, An update on the development of techniques for the determination and modelling of the impact behaviour of adhesives and bonded structures used in the automotive sector, Proceedings of the Institution of Mechanical Engineers, Part D: Journal of Automobile Engineering, 237 (2022) 095440702211359.
http://dx.doi.org/10.1177/09544070221135902

[4] L.E. Aparicio, S. Ito, H. Hashizume, Comparison of shear strength and failure mechanisms of lap joint between REBCO tapes bonded by different joining techniques, Fusion Engineering and Design, 136 (2018) 1196-1201.
https://doi.org/10.1016/j.fusengdes.2018.04.101

[5] J. Wu, H. Yong, B. Zhou, J. Liu, Numerical simulation of damage in single-lap and bridge joints of superconducting tapes based on peridynamics, Cryogenics, 151 (2025) 104159. https://doi.org/10.1016/j.cryogenics.2025.104159

[6] B. Watson, Y. Nandwani, M.J. Worswick, D.S. Cronin, Metallic multi-material adhesive joint testing and modeling for vehicle lightweighting, International Journal of Adhesion and Adhesives, 95 (2019) 102421.
https://doi.org/10.1016/j.ijadhadh.2019.102421

[7] Y. Du, L. Shi, Effect of vibration fatigue on modal properties of single lap adhesive joints, International Journal of Adhesion and Adhesives, 53 (2014) 72-79. https://doi.org/10.1016/j.ijadhadh.2014.01.007

[8] S.Y. Park, W.J. Choi, B.C. Yoon, Analysis of effects of process factors on corrosion resistance of adhesive bonded joints for aluminum alloys, Journal of Materials Processing Technology, 276 (2020) 116412.
https://doi.org/10.1016/j.jmatprotec.2019.116412

[9] F. Sun, R. Shi, S. Li, Y. Zhao, J. Min, Performance comparison of Zn, Zn-Al and Zn-Al-Mg coatings on the corrosion resistance of galvanized steel joints bonded using a hot-curing epoxy adhesive, Thin-Walled Structures, 211 (2025) 113128. http://dx.doi.org/10.1016/j.tws.2025.113128

[10] M. Goland, E. Reissner, The Stresses in Cemented Joints, Journal of Applied Mechanics, 11 (1944) A17-A27. http://dx.doi.org/10.1115/1.4009336

[11] L.J. Hart-Smith, Adhesive-Bonded Single-Lap Joints, NASA Langley Research Center, Report NASA[74]CR-112236 (1973).

[12] D.W. Oplinger, Effects of adherend deflections in single lap joints, International Journal of Solids and Structures, 31 (1994) 2565-2587.
http://dx.doi.org /10.1016/0020-7683(94)90037-X

[13] R. Adams, N. Peppiatt, Stress Analysis of Adhesive-Bonded Lap Joints, The Journal of Strain Analysis for Engineering Design, 9 (1974) 185-196. http://doi.org/10.1243/03093247V093185
[14] R. Adams, V. Mallick, A Method for the Stress Analysis of Lap Joints, Journal of Adhesion - J ADHES, 38 (1992) 199-217. http:// doi.org/10.1080/00218469208030455
[15] A. Langella, R. Carbone, L. Nele, M. Rosolia, An analytical closed-form model to evaluate the peel and shear stresses in middle plane for adhesively bonded composite single-lap joints, Journal of Composite Materials, 46 (2012) 3-17. http:// doi.org/10.1177/0021998311401113
[16] W.E. Guin, J. Wang, Theoretical model of adhesively bonded single lap joints with functionally graded adherends, Engineering Structures, 124 (2016) 316-332. http:// doi.org/j.engstruct.2016.06.036
[17] N. Stein, H. Mardani, W. Becker, An efficient analysis model for functionally graded adhesive single lap joints, International Journal of Adhesion and Adhesives, 70 (2016) 117-125. https://doi.org/10.1016/j.ijadhadh.2016.06.001
[18] O. Doeva, P.K. Masjedi, P.M. Weaver, Static deflection of fully coupled composite Timoshenko beams: An exact analytical solution, European Journal of Mechanics - A/Solids, 81 (2020) 103975. https://doi.org/10.1016/j.euromechsol.2020.103975
[19] E. Barbieri, Analytical solution of the cantilevered elastica subjected to a normal uniformly distributed follower load, International Journal of Solids and Structures, 202 (2020) 486-494. https://doi.org/10.1016/j.ijsolstr.2020.06.031
[20] C. Tang, G. Dui, Y. Fu, Elasticity solutions for functionally graded beams with arbitrary distributed loads, Composite Structures, 351 (2025) 118578. https://doi.org/10.1016/j.compstruct.2024.118578
[21] W.-Y. Huang, C. Hwu, C.-W. Hsu, Explicit analytical solutions for arbitrarily laminated composite beams with coupled stretching-bending and transverse shear deformation, European Journal of Mechanics - A/Solids, 103 (2024) 105147. https://doi.org/10.1016/j.euromechsol.2023.105147
[22] Y. Huang, Z.-Y. Ouyang, Exact solution for bending analysis of two-directional functionally graded Timoshenko beams, Archive of Applied Mechanics, 90 (2020) 1005-1023. http:// doi.org/10.1007/s00419-019-01655-5
[23] Z. Liu, Y. Huang, Z. Yin, S. Bennati, P.S. Valvo, A general solution for the two-dimensional stress analysis of balanced and unbalanced adhesively bonded joints, International Journal of Adhesion and Adhesives, 54 (2014) 112-123. https://doi.org/10.1016/j.ijadhadh.2014.05.011
[24] T.H. Nguyen, P. Le Grognec, Analytical and numerical simplified modeling of a single-lap joint, International Journal of Adhesion and Adhesives, 108 (2021) 102827. https://doi.org/10.1016/j.ijadhadh.2021.102827
[25] L. Le, L. To, N. Nguyen, S. Khatir, S. Tiachacht, l. cuong, A Solution of Plane Stress Problem Subjected to Horizontal Shear Force by Using Polynomial Airy Stress Function, Journal of Materials and Engineering Structures, 8 (2021).
[26] C. Yang, Y. Kim, S. Ryu, G.X. Gu, Prediction of composite microstructure stress-

785 strain curves using convolutional neural networks, Materials & Design, 189 (2020)
786 108509. https://doi.org/10.1016/j.matdes.2020.108509
787 [27] X. Ding, X. Hou, M. Xia, Y. Ismail, J. Ye, Predictions of macroscopic mechanical
788 properties and microscopic cracks of unidirectional fibre-reinforced polymer
789 composites using deep neural network (DNN), Composite Structures, 302 (2022)
790 116248. https://doi.org/10.1016/j.compstruct.2022.116248
791 [28] C. Wang, Z. Zhang, X. Jing, Z. Yang, W. Xu, Optimization of multistage
792 femtosecond laser drilling process using machine learning coupled with molecular
793 dynamics, Optics & Laser Technology, 156 (2022) 108442.
794 https://doi.org/10.1016/j.optlastec.2022.108442
795 [29] Z. Zhang, S. Liu, Y. Zhang, C. Wang, S. Zhang, Z. Yang, W. Xu, Optimization of
796 low-power femtosecond laser trepan drilling by machine learning and a high-
797 throughput multi-objective genetic algorithm, Optics & Laser Technology, 148 (2022)
798 107688. https://doi.org/10.1016/j.optlastec.2021.107688
799 [30] Z. Wang, J. Li, Y. Yuan, S. Zhang, W. Hu, J. Ma, J. Tan, Digital-twin-enabled online
800 wrinkling monitoring of metal tube bending manufacturing: A multi-fidelity approach
801 using forward-convolution-GAN, Applied Soft Computing, 171 (2025) 112684.
802 https://doi.org/10.1016/j.asoc.2024.112684
803 [31] Z. Gu, X. Ding, X. Hou, J. Ye, A genetic evolved machine learning approach for
804 3D DEM modelling of anisotropic materials with full consideration of particulate
805 interactions, Composites Part B: Engineering, 250 (2023) 110432.
806 https://doi.org/10.1016/j.compositesb.2022.110432
807 [32] Z. Gu, Y. Liu, D.J. Hughes, J. Ye, X. Hou, A parametric study of adhesive bonded
808 joints with composite material using black-box and grey-box machine learning methods:
809 Deep neuron networks and genetic programming, Composites Part B: Engineering, 217
810 (2021) 108894. https://doi.org/10.1016/j.compositesb.2021.108894
811 [33] M. Raissi, P. Perdikaris, G.E. Karniadakis, Physics-informed neural networks: A
812 deep learning framework for solving forward and inverse problems involving nonlinear
813 partial differential equations, Journal of Computational Physics, 378 (2019) 686-707.
814 https://doi.org/10.1016/j.jcp.2018.10.045
815 [34] S. Tang, X. Feng, W. Wu, H. Xu, Physics-informed neural networks combined with
816 polynomial interpolation to solve nonlinear partial differential equations, Computers &
817 Mathematics with Applications, 132 (2023) 48-62.
818 https://doi.org/10.1016/j.camwa.2022.12.008
819 [35] Y. Guo, X. Cao, B. Liu, M. Gao, Solving Partial Differential Equations Using Deep
820 Learning and Physical Constraints, Applied Sciences, 10 (2020) 5917.
821 https://doi.org/10.3390/app10175917
822 [36] S. Lin, Y. Chen, A two-stage physics-informed neural network method based on
823 conserved quantities and applications in localized wave solutions, Journal of
824 Computational Physics, 457 (2022) 111053. https://doi.org/10.1016/j.jcp.2022.111053
825 [37] Z. Yang, S.-K. Lai, Z. Chen, J. Fu, An augmented physics-informed neural network
826 approach with trainable scaling for nonlinear dynamic analysis, Engineering

827 Applications of Artificial Intelligence, 168 (2026) 113991.
828 https://doi.org/10.1016/j.engappai.2026.113991
829 [38] Z. Chen, Z. Yang, Y. Zhang, C. Liu, Z. Yang, S.-K. Lai, A novel Fourier time-
830 sequential PINN approach for multi-frequency analysis of nonlinear aerothermoelastic
831 problems, Advanced Engineering Informatics, 72 (2026) 104446.
832 https://doi.org/10.1016/j.aei.2026.104446
833 [39] H. Li, Y. Miao, Z.S. Khodaei, M.H. Aliabadi, Finite-PINNS: A physics-informed
834 neural network with finite geometric encoding for solid mechanics, Journal of the
835 Mechanics and Physics of Solids, 203 (2025) 106222.
836 https://doi.org/10.1016/j.jmps.2025.106222
837 [40] J. Bai, T. Rabczuk, A. Gupta, L. Alzubaidi, Y. Gu, A physics-informed neural
838 network technique based on a modified loss function for computational 2D and 3D solid
839 mechanics, Computational Mechanics, 71 (2023) 543-562.
840 http://dx.doi.org/10.1007/s00466-022-02252-0
841 [41] E. Haghighat, M. Raissi, A. Moure, H. Gomez, R. Juanes, A physics-informed deep
842 learning framework for inversion and surrogate modeling in solid mechanics, Computer
843 Methods in Applied Mechanics and Engineering, 379 (2021) 113741.
844 https://doi.org/10.1016/j.cma.2021.113741
845 [42] T. Le-Duc, S. Lee, H. Nguyen-Xuan, J. Lee, A hierarchically normalized physics-
846 informed neural network for solving differential equations: Application for solid
847 mechanics problems, Engineering Applications of Artificial Intelligence, 133 (2024)
848 108400. https://doi.org/10.1016/j.engappai.2024.108400
849 [43] C. Rao, H. Sun, Y. Liu, Physics-Informed Deep Learning for Computational
850 Elastodynamics without Labeled Data, Journal of Engineering Mechanics, 147 (2021)
851 04021043. https://doi.org/10.1061/(ASCE)EM.1943-7889.0001947
852 [44] X. Tian, J. Wang, C.-W. Kim, X. Deng, Y. Zhu, Automated machine learning exact
853 dirichlet boundary physics-informed neural networks for solid mechanics, Engineering
854 Structures, 330 (2025) 119884. https://doi.org/10.1016/j.engstruct.2025.119884
855 [45] Y. Li, D. Wan, Z. Wang, D. Hu, Physics-constrained deep learning approach for
856 solving inverse problems in composite laminated plates, Composite Structures, 348
857 (2024) 118514. https://doi.org/10.1016/j.compstruct.2024.118514
858 [46] W. Hu, H. Cheng, C. Wang, L. He, K. Zhang, Y. Li, B. Liang, A micromechanical
859 solving method integrating the physics-informed neural network with the self-
860 consistent cluster analysis method for composites laminate, Composite Structures, 368
861 (2025) 119264. https://doi.org/10.1016/j.compstruct.2025.119264
862 [47] H. Hu, L. Qi, X. Chao, Physics-informed Neural Networks (PINNs) for
863 computational solid mechanics: Numerical frameworks and applications, Thin-Walled
864 Structures, 205 (2024) 112495. https://doi.org/10.1016/j.tws.2024.112495
865 [48] X, Han, Y, Chao, W, Zhang, Y, Chao, C, Wu. Study on the effect of post curing on
866 the mode II fracture energy of structural adhesive using a parameter identification
867 approach. International Journal of Adhesion and Adhesives, 95 (2019) 102398.
868 https://doi.org/10.1016/j. ijadhadh.2019.102398.